

Contents lists available at ScienceDirect

Journal of Computational and Applied Mathematics

journal homepage: www.elsevier.com/locate/cam



Multiscale model reduction for pore-scale simulation of Li-ion batteries using GMsFEM



Maria Vasilyeva ^{a,b,*}, Aashutosh Mistry ^c, Partha P. Mukherjee ^c

- ^a Institute for Scientific Computation, Texas A&M University, College Station, TX 77843, USA
- ^b North-Eastern Federal University, Yakutsk, 677980, Republic of Sakha (Yakutia), Russia
- ^c School of Mechanical Engineering, Purdue University, West Lafayette, IN 47907, USA

ARTICLE INFO

Article history: Received 4 October 2017 Received in revised form 4 May 2018

Keywords: Multiscale method GMsFEM Electrochemical processes Pore-scale simulation Lithium-ion batteries

ABSTRACT

In this work, we consider electrochemical processes for the pore-scale simulation of Lithium-ion batteries (LIBs). Mathematical model consists of the coupled system of the equations for the concentration and electric potential. We develop fine-scale approximation using discontinuous Galerkin approach, where interface condition is imposed weakly. We present novel multiscale model reduction technique based on the GMsFEM, where multiscale basis functions are constructed using information about variation of the medium at the micro level. We present numerical results for two cases of the boundary conditions and compare errors for different coarse grids for testing the proposed computational multiscale method. Numerical results show that the multiscale basis functions can efficiently capture the information of the fine-scale features of the medium with significant dimension reduction of the system and provide accurate solutions.

© 2018 Elsevier B.V. All rights reserved.

0. Introduction

Lithium-ion is one of the most successful energy storage chemistry [1–4]. Ever since its conceptualization in 80s, it has undergone multiple modifications both for the materials [5] as well as electrode microstructure [6,7]. It has replaced many of its predecessor secondary batteries for small electronics applications and now the electric vehicles are knocking on our doorstep. From an end user perspective, three aspects are of considerable importance [8]:

- 1. Performance describes the voltage, capacity and energy density of the battery,
- 2. Durability is related to cycle life and rechargeability [9,10],
- 3. Safety concerns the fire hazard if these batteries are mishandled [11] (e.g., mechanical abuse, thermal abuse, etc.).

Mathematical modeling of the cell response to various operating conditions as well as stressers is of extreme importance since it provides both predictive capabilities as well as a fundamental understanding of the cell level transport processes. Such an insight leads to innovative solutions.

Consider Fig. 1(a) where a unit cell of LIB is schematically shown. The cell comprises of two (porous) electrodes separated by a fibrous separator. Both the electrodes as well as separator are kept porous to ensure ionic transport from one electrode to the other (electrolyte is filled in these pores). Electrons flow in external circuit, while internally charge conservation is ensured by equal amount of ionic current (Li⁺ ion is the major charge carrier in electrolyte). Li is stored in electrode material (also referred to as *active material*) via intercalation reaction. This electrode active materials are chosen such that

^{*} Corresponding author at: Institute for Scientific Computation, Texas A&M University, College Station, TX 77843, USA. E-mail addresses: vasilyevadotmdotv@gmail.com (M. Vasilyeva), mistrya@purdue.edu (A. Mistry), pmukherjee@purdue.edu (P.P. Mukherjee).

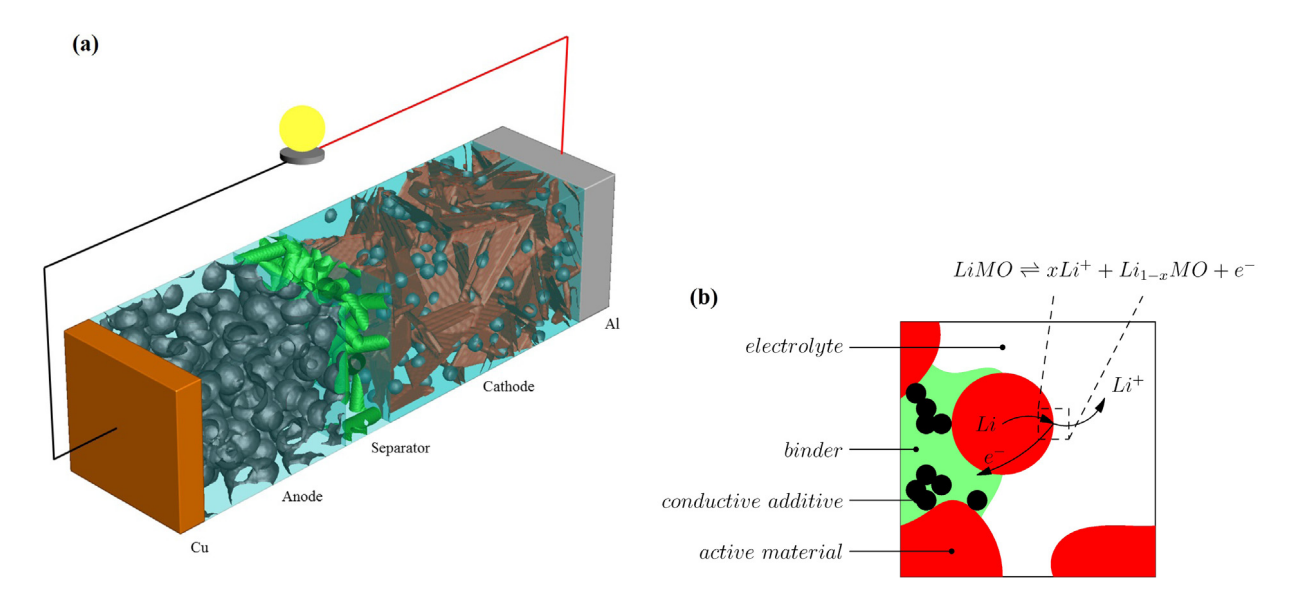


Fig. 1. (a) A unit cell of Lithium ion battery contains a fibrous (electronically insulating) separator sandwiched between two porous electrodes. e^- are charge carriers in the external circuit, while internally ionic species complete the electric circuit. On anode side, copper (Cu) is used as current collector, while at cathode aluminum (Al) is employed. (b) Illustrating various transport processes at pore-scale. Deintercalating Li at active material–electrolyte interface generates Li⁺ ion in the electrolyte phase and e^- in the solid phase (subfigure (b) is adapted from [12], subfigure (a) is borrowed from [13]).

(1) the two materials lead to as high voltage difference as possible as well as (2) the materials have higher Li storage capacity. Usual choice of anode material is graphite, while cathode contains transition metal oxides (e.g., Nickel Manganese Cobalt Oxide, $\text{LiNi}_{1/3}\text{Mn}_{1/3}\text{Co}_{1/3}\text{O}_2$). Most of the active materials suitable for cathode have very poor electronic conductivity, hence conductive additive (e.g., carbon black) are introduced to the cathode. Moreover, polymeric binder is used to ensure sufficient bonding among electrode constitutences as well as between electrode and current collectors. Fig. 1(a) displays such a composite cathode.

Fundamental understanding of such processes relies heavily on pore-scale structure of the electrode (Fig. 1(b)), and highlights the importance of such a detailed simulation. Finite element based pore-scale simulations are constructed and analyzed by the COMSOL Multiphysics package [14–16]. For performing of the fine-scale simulation, we can use open-source software components, for example, FEniCS [17]. FEniCS components provide scientific computing tools for working with computational meshes, finite-element variational formulations and numerical linear algebra. For simulation of the processes with discontinuous solution, the discontinuous finite element method can be used. Using discontinuous finite element method, we can impose nonlinear interface condition weakly [18]. We note, that various finite volume or finite element based approximation can be used for pore-scale simulations with domain decomposition methods [19–21].

For a pore-scale simulation we should use a computational grid that resolve all small heterogeneities. This leads to the very large system of discrete equations and for such problems a numerical homogenization (porous electrode theory) or multiscale method should be used. Traditionally, the electrochemical (and electrochemical-thermal) response of LIBs is modeled using the porous electrode theory [22–24]. In such an account of the physicochemical behavior, it is assumed that the electrode sample is large enough to contain statistically significant amount of heterogeneity of material phase structure (i.e., arrangement of active material, conductive additives and binder) and hence homogenization approximation [25] can be made and the electrode structure can be represented in terms of a smaller list of descriptors (i.e., porosity, tortuosity, etc.). While this approach has been extensively used so far [26,12], it cannot explain many observable, especially those which are associated with smaller length scales than the electrode dimensions, and usually ad-hoc modifications have been made to explain those. A few of such limitations can be enumerated as follows:

- 1. Porous electrode theory for LIBs assumes that the active material particles are spherical and isotropic. This is a very stringent assumption since many materials have non-spherical particle geometries and many electrode materials exhibit considerable anisotropy [7,27]. Moreover, as outlined earlier, the composite electrode contains inactive solid species (conductive additive and binder). The treatment of these secondary solids is quite primitive and does not account for relative arrangement of different phases [28–30].
- 2. Local heterogeneity in the electrode structure [31,32] is argued to lead to cell degradation and failure (e.g., heat spots). Moreover, interface scale processes such as *lithium plating* and *solid electrolyte interphase* growth and/or fracture cannot be accurately modeled using this porous electrode description [33–36].

The construction of the porous electrode model is based on the homogenization theory. The theory of the macroscopic description of porous electrodes is described by Newman [25,37]. The porous electrode is treated as a superposition of

continuous electrode and solution phases, each of known volume fraction. In this method, they did not consider the detailed pore geometry but, instead, describe the porous electrode by its specific interfacial area and volume fractions of each phase. As there exists interface between the two phases at each point in the volume of the electrode, the electrochemical reaction at the surface becomes a homogeneous reaction term in the species material balance [25,38].

Derivation of the micro–macro LIB models using asymptotic expansions and mathematical tools from homogenization theory was presented in [37], where they consider periodic case. This asymptotic homogenization based model and similar in nature to the one developed in Newman's model for LIB. In the paper [39] the authors apply the homogenization theory to derive macroscopic battery model for periodic geometry and performs numerical experiments.

As in homogenization method, for extracting microstructure information we perform calculation in local domains and use local solutions as a multiscale basis function. Using GMsFEM, we successfully construct a coupled micro-macroscale model, where all micro-scale calculations are performed offline (only once, before calculations) in the local domains and take into account microstructure heterogeneity. We have run a series of numerical simulations for different number of multiscale basis functions on a different coarse grid. The results of the simulations show good agreement between the multiscale and the fine-scale solutions.

For the approximation on the coarse grid, we develop the multiscale model reduction for electrochemical problems in LIBs based on the Generalized Multiscale Finite Element Method (GMsFEM), where we construct multiscale basis functions by the solution of the local spectral problems in local domains $K = K_s \cup K_e$, where K_e and K_s are the electrolyte and solid (anode and cathode) subdomains. Multiscale basis functions have discontinuity on the interface and take into account a possible complex microstructure i.e. use information about variation of the solid medium in the micro level. In this method, by taking larger number of the multiscale basis functions, we reduce errors. For coarse-scale coupling, we use discontinuous Galerkin method, that gives several advantages: (1) the construction of the multiscale basis functions can be performed in non-overlapping local domains, (2) it avoids partition of unity functions, (2) as partitioning to the local domains we can use any shapes of the local domains. In general, we can improve the accuracy of our approach by using adaptivity and online techniques [40,41]. For the real world 3D problems, a high performance computation can be used, where construction of the coarse-scale system and local problem solutions can be carried out in parallel with very high efficiency of parallelization.

The paper contains three sections. In the first section, we consider mathematical model for a pore-scale simulations of Li-ion batteries. In Section 2, we develop fine-scale approximation using discontinuous Galerkin method and present multiscale model reduction using GMsFEM. Next in Section 3, we present the results of the numerical simulations and perform sensitivity analysis for the multiscale solver with respect to the numbers of multiscale basis functions on a different coarse grid and finally present conclusions.

1. Mathematical description of Li-ion batteries

1.1. Electrochemical processes

Electrochemical response of Li-ion cells comprises of coupled multiphase transport processes. It includes conservation of intercalated Li in active material (solid) phase, conservation of Li^+ ions in the electrolyte phase, conservation of e^- in solid phase (charge carriers in solid phase) and conservation of ionic charge in electrolyte phase. These four processes are mathematically described by four partial differential equations [22,24,42]:

Li conservation in solid phase (active material)

$$\frac{\partial c_s}{\partial t} = \nabla \cdot (D_s \nabla c_s) \tag{1}$$

Li⁺ conservation in electrolyte phase

$$\frac{\partial c_e}{\partial t} = \nabla \cdot (D_e \nabla c_e) \tag{2}$$

e⁻ conservation in solid phase

$$-\nabla \cdot (\kappa_s \nabla \phi_s) = 0. \tag{3}$$

Charge conservation in electrolyte phase

$$-\nabla \cdot (\kappa_{\rho} \nabla \phi_{\rho}) + \nabla \cdot (\kappa_{D} \nabla c_{\rho}) = 0. \tag{4}$$

Total ionic flux j_e and diffusional conductivity κ_D are described by the following relations, while the remaining transport coefficients are explained in the following table.

$$j_e = -\kappa_e \nabla \phi_e - \kappa_D \nabla c_e \tag{5}$$

$$\frac{\kappa_D}{\kappa_e} = -\frac{1 - t_+}{F} \frac{RT}{c}. \tag{6}$$

Table 1A listing of various physical properties and their functional relations, used in the present set of simulations [21,39,42].

Property	Value and/or function	Units
Anode, Ω_a		
$U_0(c_a)$	$\exp(-10 c_a/c_{a,max})$	V
$c_{a,max}$	0.024681	mol/cm ³
$c_{a,0}$	$0.2 c_{a,max}$	mol/cm ³
D_a	3.9×10^{-10}	cm ² /s
κ_a	1.0	S/cm
Cathode, Ω_c		
$U_c(c_c)$	$4-100(c_c/c_{c,max}-0.5)^5$	V
$c_{c,max}$	0.023671	mol/cm ³
$c_{c,0}$	$0.8 c_{c,max}$	mol/cm ³
D_c	1.0×10^{-9}	cm ² /s
κ_c	0.038	S/cm
Electrolyte, Ω_e		
C _{e,0}	0.001	mol/cm ³
D_e	7.5×10^{-7}	cm ² /s
κ_e	0.002	S/cm

Roman Syr	mbols					
С	Concentration field (mol/cm³)					
D	Diffusivity (cm ² /s)					
F	Faraday's constant (96 487 C/mol)					
İı	Butler–Volmer current density (A/cm ²)					
\hat{n}_I	Unit normal, pointing from solid to electrolyte phase					
R	Universal Gas constant (8.314 J/mol·K)					
T	Absolute temperature (298 K)					
t^+	Transference number (0.363 (dimensionless))					
Greek Sym	ibols					
φ	Electric potential (V)					
κ	Electrolyte conductivity (S/cm)					
κ_D	Diffusional conductivity (A/cm ³)					
Superscrip	t/subscript					
e	Electrolyte phase property					
S	Solid phase property					
а	Anode property					
С	Cathode property					
Abbreviatio	ons					
IPDG	Interior Penalty Discontinuous Galerkin method					
LIB	Lithium Ion Battery					
NMC	Nickel Manganese Cobalt Oxide					
PDE	Partial Differential Equation					
GMsFEM	Generalized Multiscale Finite Element Method					

Let $\Omega = \Omega_s \cup \Omega_e$ be the computational domain, where Ω_s and Ω_e are the subdomains for the electrodes and electrolyte, respectively. The electrodes domain contains two subdomains, $\Omega_s = \Omega_a \cup \Omega_c$, where Ω_a and Ω_c are the subdomains for the anode and cathode. Therefore, a coupled system of the equations for the concentration and electric potential, we can write in the following general form [19,20,42]

$$\frac{\partial c}{\partial t} - \nabla(D\nabla c) = 0, \quad \text{in } \Omega,
-\nabla(\kappa\nabla\phi + \kappa_D\nabla c) = 0, \quad \text{in } \Omega,$$
(7)

where

$$D = \begin{cases} D_e \text{ in } \Omega_e \\ D_a \text{ in } \Omega_a \\ D_c \text{ in } \Omega_c, \end{cases} \qquad \kappa = \begin{cases} \kappa_e \text{ in } \Omega_e \\ \kappa_a \text{ in } \Omega_a \\ \kappa_c \text{ in } \Omega_c, \end{cases} \qquad \kappa_D = \begin{cases} -\kappa_e \frac{1 - t_+}{F} \frac{RT}{c} \nabla c \text{ in } \Omega_e \\ 0 \text{ in } \Omega_a \\ 0 \text{ in } \Omega_c. \end{cases}$$

We set initial condition for concentration $c = c_0(x)$ in Ω . Simulation parameters are presented in Table 1.

1.2. Interface conditions

In addition to these conservation statements, one needs a relation for intercalation flux at active material–electrolyte interface (a constitutive relation). For electrode materials employed in LIBs, Butler–Volmer reaction kinetics (Eq. (8)) is found to be a very accurate description for this charge transfer at active material–electrolyte interface Γ_I

$$j_{I} = k\sqrt{c_{s}c_{e}\left(c_{s,max} - c_{s}\right)}\left(\exp\left(\frac{F\eta}{2RT}\right) - \exp\left(-\frac{F\eta}{2RT}\right)\right),\tag{8}$$

where $\eta = \phi_s - \phi_e - U_0(c)$ is the overpotential and U_0 is the solid open circuit voltage.

Consider Fig. 1(b) where this charge transfer is schematically illustrated. For a generic metal oxide (MO) active material, Li deintercalation leads to consumption of Li in solid phase, generation of Li⁺ in electrolyte phase and generation of e^- in solid phase. Since conventional current is described by the direction of flow of positive charge carriers, generation of e^- is equivalent to consumption of charge in the solid phase. Given this physical description, the above described transport processes (Eqs. (1)–(4)) are mutually coupled via interface conditions shown below (here \hat{n}_l represents local surface normal pointing from solid to electrolyte phase):

Li flux at solid-electrolyte interface

$$-D_s \nabla c_s \cdot \hat{n}_I = \frac{j_I}{F} \tag{9}$$

Li⁺ flux at solid–electrolyte interface

$$-D_e \nabla c_e \cdot \hat{n}_I = \frac{j_I}{F} \tag{10}$$

e⁻ flux at solid-electrolyte interface

$$-\kappa_s \nabla \phi_s \cdot \hat{n}_l = j_l. \tag{11}$$

Total ionic flux at solid-electrolyte interface

$$-\kappa_e \nabla \phi_e \cdot \hat{n}_l - \kappa_D \nabla c_e \cdot \hat{n}_l = j_l. \tag{12}$$

1.3. Boundary conditions

The boundaries of the LIB unit cell are impervious to species flow. This leads to the following form of boundary conditions for Li and ${\rm Li^+}$ concentration:

for Li conservation in active material

$$-D_s \nabla c_s \cdot \hat{n}_h = 0 \text{ on } \Gamma_a \cup \Gamma_c \tag{13}$$

for Li⁺ conservation in electrolyte

$$-D_e \nabla c_e \cdot \hat{n}_b = 0 \text{ on } \Gamma_e. \tag{14}$$

Here $\partial \Omega = \Gamma_a \cup \Gamma_c \cup \Gamma_e$ and \hat{n}_b represents unit normal at the boundary, pointing outward.

The corresponding boundary condition for the potential equations is:

$$\phi_a = g_a, \quad \text{on } \Gamma_a$$
 $-\kappa_c \nabla \phi_c \cdot \hat{n}_b = j_{app}, \quad \text{on } \Gamma_c$
 $-\kappa_c \nabla \phi_c \cdot \hat{n}_b = 0, \quad \text{on } \Gamma_c.$

Current density j_{app} is expressed in terms of C-rate (e.g., [30,35]). C-rate can be understood as non-dimensional current density. Its alternative definition is related to theoretical time of operation in hours [22], for example, if a battery operating at 2 C current would theoretically operate for 1/2 h, which in turn is related to theoretical capacity of electrodes. Since most of the commercial LIBs are cathode limited, cathode capacity is used to compute C-rate [43].

Let $|\Omega_c|$ be volume of cathode and $c_{c,0}$ is the initial uniform cathode concentration. This cathode can be discharged till cathode concentration reaches the maximum value, i.e., $c_{c,max}$. Thence, total cathode capacity is:

$$Q_c = \frac{F\left(c_{c,max} - c_{c,0}\right) |\Omega_c|}{3600} \tag{Ah}.$$

If A_{ccc} is the cross-sectional area of current collector on the cathode side, using Eq. (15), corresponding current density becomes:

$$j_{app} = \frac{Crate \cdot Q_c}{A_{crc}} \qquad (A/cm^2). \tag{16}$$

2. Computational methodology

2.1. Fine-scale approximation using DG method

For approximation by space, we use discontinuous Galerkin method (IPDG) [44,45]. Let \mathcal{T}_h be a finite element partition of the domain and Γ_0 be the set of all interior faces. Let e be the edge between elements K_1 and K_2 , then the jump and average of a scalar function e and for vector function e are given by

$$\{v\} = \frac{v_{K_1} + v_{K_2}}{2}, \quad [v] = v_{K_1} - v_{K_2},$$

$$\{u \cdot n\} = \frac{u_{K_1} n_{K_1} + u_{K_2} n_{K_2}}{2}, \quad [u \cdot n] = u_{K_1} n_{K_1} - u_{K_2} n_{K_1}.$$

For approximation by time we will use implicit scheme with

$$\frac{\partial c}{\partial t} \approx \frac{c - \check{c}}{\tau},$$

where τ is the time step and \check{c} is the solution from previous time.

The weak formulation of the Problem (7) for Interior Penalty Discontinuous Galerkin method (IPDG) is given by

$$m_c(c, q) + a_c^{DG}(c, q) + d_c^{IC}(c, q) = m_c(\check{c}, q),$$
 (17)

with

$$m_{c}(c,q) = \frac{1}{\tau}(c,q),$$

$$a_{c}^{DG}(c,q) = \sum_{K \in \mathcal{T}^{h}} \int_{K} D\nabla c \cdot \nabla q dx - \sum_{e \in \Gamma_{0}/\Gamma_{l}} \int_{e} \{D\nabla c \cdot n\}[q] ds - \sum_{e \in \Gamma_{0}/\Gamma_{l}} \int_{e} \{D\nabla q \cdot n\}[c] ds$$

$$+ \gamma \sum_{e \in \Gamma_{0}/\Gamma_{l}} \int_{e} D[c][q] ds,$$

$$(18)$$

 $d_c^{IC}(c,q) = \sum_{e \in \Gamma_I} \int_e \frac{1}{F} j_I(c,\phi)[q] ds,$

for concentration and

$$a_{\phi}^{DG}(\phi, v) + g_{\phi}^{IC}(\phi, v) - b_{\phi}^{DG}(c, v) = l_{\phi}(v), \tag{19}$$

with

$$a_{\phi}^{DG}(\phi, v) = \sum_{K \in \mathcal{T}^{h}} \int_{K} \kappa \nabla \phi \cdot \nabla v dx - \sum_{e \in \Gamma_{0}/\Gamma_{1}} \int_{e} \{\kappa \nabla \phi \cdot n\}[v] ds - \sum_{e \in \Gamma_{0}/\Gamma_{1}} \int_{e} \{\kappa \nabla v \cdot n\}[\phi] ds + \gamma \sum_{e \in \Gamma_{0}/\Gamma_{1}} \int_{e} \kappa [\phi][v] ds,$$

$$b_{\phi}^{DG}(c, v) = \sum_{K \in \mathcal{T}^{h}} \int_{K} \kappa_{D} \nabla c \nabla v dx - \sum_{e \in \Gamma_{0}/\Gamma_{1}} \int_{e} \{\kappa_{D} \nabla c \cdot n\}[v] ds - \sum_{e \in \Gamma_{0}/\Gamma_{1}} \int_{e} \{\kappa_{D} \nabla v \cdot n\}[c] ds + \gamma \sum_{e \in \Gamma_{0}/\Gamma_{1}} \int_{e} \kappa_{D}[c][v] ds,$$

$$g_{\phi}^{IC}(\phi, v) = \sum_{e \in \Gamma_{0}} \int_{e} j_{I}(c, \phi)[v] ds, \quad l_{\phi}(v) = \sum_{e \in \Gamma_{0}} \int_{e} j_{app} v ds,$$

$$(20)$$

for potential. Here using DG method we impose the interface conditions weakly, Γ_0 is the interior edges and γ is the penalty term.

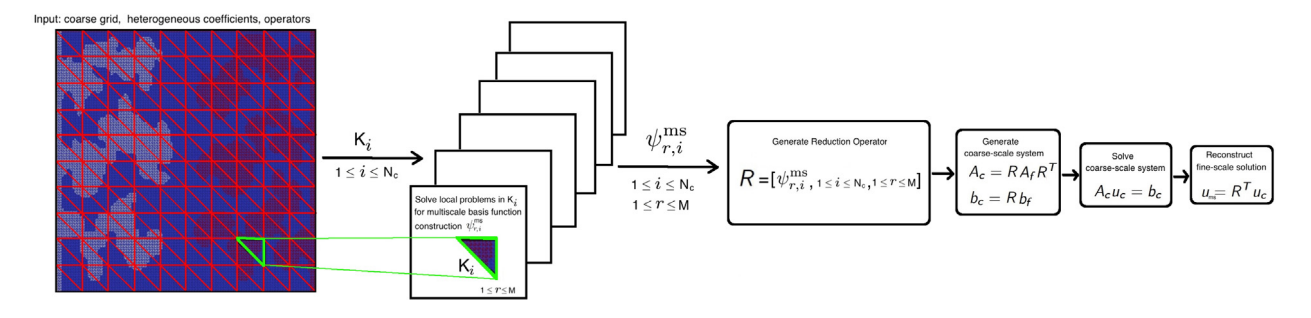


Fig. 2. Schematic illustration of the multiscale method.

For linearization, we take concentration from the previous time step in concentration equation. Then we have following computational algorithm:

1. Solve concentration equation

$$m_c(c, q) + a_c^{DG}(c, q) = f_c(q), \quad f_c(q) = m_c(\check{c}, q) - d_c^{IC}(\check{c}, q),$$

2. Solve nonlinear equation for the potential

$$a_\phi^{DG}(\phi,v)+g_\phi^{IC}(\phi,v)=f_\phi(v), \quad f_\phi(v)=l_\phi(v)+b_\phi^{DG}(c,v).$$

Note that, because we used linearization from previous time step for concentration, our system of equations is decoupled. We can write system of equations in the matrix form

- For the concentration: $(M_f^c + A_f^c)c = Q_f^c$, For the potential: $F_f(\phi) = 0$, $F_f(\phi) = Q_f^\phi (A_f^\phi + G_f^\phi(\phi))\phi$,

where M_H^c and A_f^c are the mass and stiffness matrices for concentration and A_f^{ϕ} is the stiffness matrix for potential, Q_f^c $M_f^c \check{c} - D_f^c \check{c}$ and $Q_f^{\phi} = g_f - B_f^{\phi} \check{c}$.

For numerical solution of the nonlinear equation for the potential, we use Newton method where in each nonlinear iteration, we solve following linear systems

$$F_f'(\phi^k)\delta\phi = F_f(\phi^k),$$

where $\phi^{k+1} = \phi^k + \delta \phi$ and k is the number of the nonlinear iteration.

2.2. Multiscale model reduction

In multiscale approach, we construct the multiscale basis functions in each coarse block to represent the local heterogeneities in each coarse region. The GMsFEM is a systematic approach to identify multiscale basis functions via local snapshots and local spectral problems. The local snapshots are constructed by solving a local problem and contain the information about local heterogeneities. By performing local spectral decomposition, the method identifies multiscale basis functions [40,46-50].

In GMsFEM, we can construct continuous or discontinuous multiscale basis functions. In continuous Galerkin approach, the local multiscale basis functions are multiplied by a partition of unity functions and multiscale basis functions are constructed via conforming boundary conditions. To avoid this, we propose the use of discontinuous Galerkin formulation. The main advantages of the IPDG framework for the GMsFEM are (1) avoids the partition of unity functions, (2) nonoverlapping partition, (3) unstructured coarse and fine meshes for complicated porous geometry.

In GMsFEM framework, we have two main stages:

Stage 1. The construction of the multiscale basis functions in local domains (offline stage).

Stage 2. The global coarse grid level coupling (online stage).

The offline stage usually contains two steps: (1) construction of a snapshot space and (2) construction of a small dimensional offline space by performing a dimension reduction of the snapshot space [51–54]. We present schematic illustration of the method in Fig. 2.

Let \mathcal{T}_H be the coarse scale partition of the domain Ω^{ε} consisting of local subdomains K, where the characteristic mesh size $H \gg h$, and h is the fine scale mesh size that is sufficiently fine to resolve the fine-scale features.

Global coupling. Let $V_H(K)$ be the local offline space, which consists of functions that are defined on coarse grid block $K \in \mathcal{T}_H$. We decompose the local offline space $V_H(K)$ into two subspaces, $V_H(K) = V_H^b(K) + V_H^i(K)$, where $V_H^b(K)$ and $V_H^i(K)$ contain boundary and interior multiscale basis functions, respectively. The global multiscale space V_H is then defined as the sum of all these $V_H(K)$, $K \in \mathcal{T}_H$.

$$V_H = \text{span}\{\psi_{r,i}^{\text{ms}}, \quad r = 1, \dots, M_i, \quad i = 1, \dots, N_c\},\$$

where M_i is the number of the multiscale basis functions in each K_i and N_c is the number of the local domains. Let V_H^c and V_H^ϕ are the finite dimensional function spaces for concentration and potential

$$V_H^c = \text{span}\{\psi_{r,i}^{c,\text{ms}}, r = 1, \dots, M_i^c, i = 1, \dots, N_c\},\$$

 $V_H^\phi = \text{span}\{\psi_{r,i}^{\phi,\text{ms}}, r = 1, \dots, M_i^\phi, i = 1, \dots, N_c\},\$

where M_i^c , M_i^ϕ are the numbers of the multiscale basis functions on each K_i and $\psi_{r,i}^{c,ms}$ and $\psi_{r,i}^{\phi,ms}$ are supported in local

In the DG-GMsFEM, we will apply the symmetric IPDG approach for the global coupling. We seek an approximation

$$c_H = \sum_{r,i} s_i \psi_{r,i}^{c,\text{ms}} \text{ in } V_H^c, \quad \text{ and } \quad \phi_H = \sum_{r,i} d_i \psi_{r,i}^{\phi,\text{ms}} \text{ in } V_H^\phi$$

such that

$$m_{c}(c_{H}, q) + a_{c}^{DG}(c_{H}, q) = m_{c}(\check{c}_{H}, q) - d_{c}^{IC}(\check{c}_{H}, q), \quad \forall q \in V_{H}^{c},$$

$$a_{\phi}^{DG}(\phi_{H}, v) + g_{\phi}^{IC}(\phi_{H}, v) = l_{\phi}(v) + b_{\phi}^{DG}(c, v), \quad \forall v \in V_{H}^{\phi}.$$
(21)

The coarse-scale system can be formed by the projection of the fine-scale matrices onto the coarse grid. The projection matrices can be assembled using the multiscale basis functions

$$R_{c} = [R_{1}^{c}, R_{2}^{c}, \dots, R_{N_{c}}^{c}], \quad R_{i}^{c} = [\psi_{1,i}^{c}, \psi_{2,i}^{c}, \dots, \psi_{M_{i}^{c},i}^{c}],$$

$$R_{\phi} = [R_{1}^{\phi}, R_{2}^{\phi}, \dots, R_{N_{c}}^{\phi}], \quad R_{i}^{\phi} = [\psi_{1,i}^{\phi}, \psi_{2,i}^{\phi}, \dots, \psi_{M_{i}^{\phi},i}^{\phi}],$$

where R_i^c and R_i^{ϕ} is the local projection matrix in a coarse element K_i . Using the projection matrix R_i , we can define the

$$(M_H^c + A_H^c)c_H = Q_H^c, \quad M_H^c = R_c^T M_f^c R_c, \quad A_H^c = R_c^T A_f^c R_c, \quad Q_H^c = R_c^T Q_f^c,$$

$$F_H' \delta \phi_H = F_H, \quad F_H' = R_A^T F_f' R_\phi, \quad F_H = R_A^T F_f,$$
(22)

where M_H and M_f are the coarse-scale and fine-scale mass matrices, A_H and A_f are the coarse-scale and fine-scale stiffness matrices. After calculating the coarse-scale solutions c_H and ϕ_H , we can recover fine-scale solutions by $c_{\rm ms}=R_{\rm c}c_H$ and $\phi_{\rm ms} = R_{\phi} \phi_H$.

For the multiscale basis functions construction, we solve spectral problems and use the eigenfunctions corresponding to the dominant eigenvalues of the spectral problem as the multiscale basis functions. The local offline space for potential or for concentration consists of two spaces $V_H^p(K) = V_H^{b,p}(K) + V_H^{i,p}(K)$ ($p = c, \phi$), where $V_H^{b,p}(K)$ is the boundary multiscale space and $V_H^{i,p}(K)$ is the interior multiscale space (see Figs. 3 and 4 for illustration). Now we present the details of constructing the boundary basis and interior basis.

Construction of the multiscale basis functions. For construction of the first multiscale space $V_H^{b,p}(K)$, we solve following local spectral problem: find ψ^b in $V_h^p(K)$ such that

$$a_p^{DG}(\psi^b, v) = \lambda s_p(\psi^b, v), \quad \forall v \in V_h^p(K), \tag{23}$$

where $s_p(u, v) = \int_{\partial K} b_p u \, v \, ds$ and

$$a_p^{DG}(u,v) = \int_K b_p \nabla u \cdot \nabla v dx - \int_{\Gamma_0/\Gamma_1} \{b_p \nabla u \cdot n\}[v] ds - \int_{\Gamma_0/\Gamma_1} \{b_p \nabla v \cdot n\}[u] ds + \gamma \int_{\Gamma_0/\Gamma_1} b_p[u][v] ds.$$

Here Γ_0 is the interior edges, $b_\phi = \kappa$ and $b_c = D$. Note that, solution of the local problem is discontinuous on the interface

To construct a reduced space $V_H^{b,p}(K)$, we select the first M_p^b eigenvectors $\psi_1^b, \psi_2^b, \ldots, \psi_{M_p^b}^b$ corresponding to the first smallest eigenvalues, $\lambda_1 \leq \lambda_2 \leq \cdots \leq \lambda_{M^p}$ and define the space $V_H^{b,p}(K)$ by

$$V_H^{b,p}(K) = \text{span}\{\psi_{1,K}, \psi_{2,K}, \dots, \psi_{M_n^b,K}\}.$$
(24)

For the construction of the second local multiscale space $V_H^{i,p}(K)$, we use following spectral problem: find ψ^i in $V_h^p(K)$ such that

$$a_p^{DG}(\psi^i, v) = \mu s_p(\psi^i, v), \quad \forall v \in V_h^p(K), \tag{25}$$

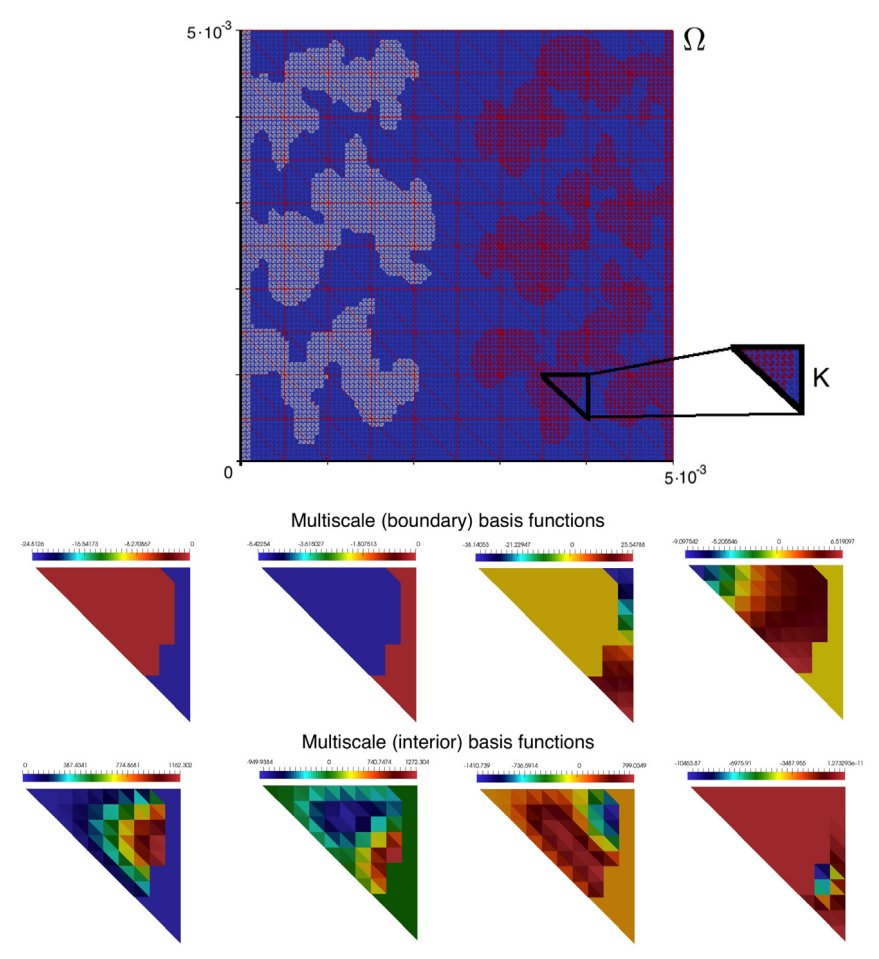


Fig. 3. Computational domain with subdomains, fine mesh, local domains and first 4 multiscale boundary and interior basis functions. Structured coarse mesh with 200 local domains.

with zero Dirichlet boundary conditions. We arrange the eigenvalues in an ascending order $\mu_1 \leq \mu_2 \leq \cdots \leq \mu_{M_n^i}$. We select the first M_p^i eigenfunctions $\psi_1^i, \psi_2^i, \dots, \psi_{M_n^i}^i$ corresponding to the first M_p^i smallest eigenvalues. The space $V_H^{i,p}(K)^i$ is spanned by these functions

$$V_H^{i,p}(K) = \operatorname{span}\{\psi_{1,K}^i, \psi_{2,K}^i, \dots, \psi_{M_{r}^i,K}^i\}.$$
(26)

The multiscale basis functions in $V_H^{i,p}(K)$ are called interior basis functions. In Figs. 3 and 4, we showed first four multiscale boundary and interior basis functions. Presented multiscale basis functions have discontinuity on interface. For reducing size of the snapshot space, we can use random boundary condition in the oversampled domain. We can also use parallel computations in coarse scale system assembling and solving system of equation.

3. Numerical results

In this section, we present results of the fine-scale and multiscale solutions. Computational domain Ω has size 5 \cdot 10^{-3} [cm] $\times 5 \cdot 10^{-3}$ [cm], where $\Omega = \Omega_e \cup \Omega_a \cup \Omega_c$. Fine mesh contains 10,201 vertices and 20,000 cells. For multiscale model reduction, we use structured and unstructured coarse meshes with different numbers of the local domains (see Figs. 3 and 4). Here, we construct multiscale basis functions only once and use them for dimension reduction of the nonlinear system. Simulation parameters are presented in Table 1.

We consider two cases with different applied current density:

Case 1:
$$j_{app} = 0.0007$$
 and $t_{max} = 2125$ s, Case 2: $j_{app} = 0.0015$ and $t_{max} = 850$ s.

and set $g_a = 0.1353$. We use Newton solver for potential equation at each time step and use 200 time steps.

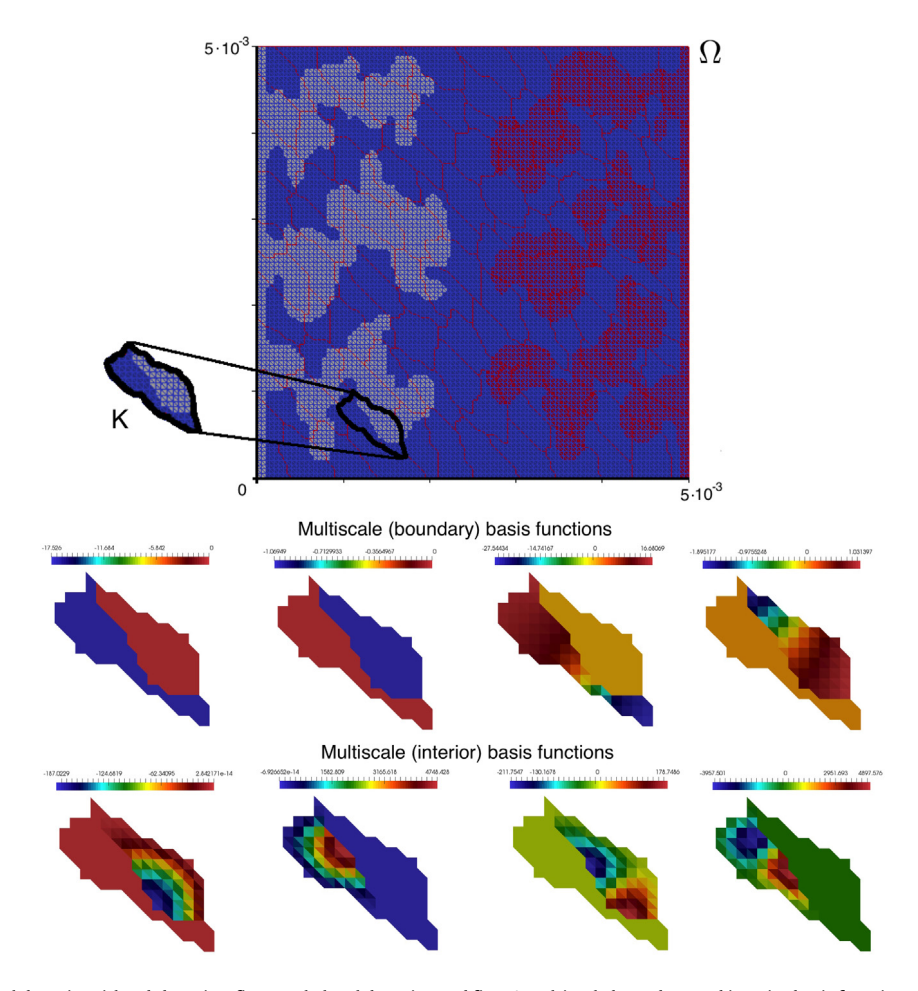


Fig. 4. Computational domain with subdomains, fine mesh, local domains and first 4 multiscale boundary and interior basis functions. Unstructured coarse mesh with 200 local domains.

Concentrations for t_m , m=10, 100 and 200 are shown at Fig. 5 for fine-scale solution. We present solutions in subdomains separately only in figures, because solution has big jump on interface, but in the numerical calculations, we solve problem in whole domain Ω . We calculate an average concentration on $\Gamma_I = \Gamma_I^a \cup \Gamma_I^c$ and cell voltage V_c

$$\langle c_a \rangle_{\Gamma_I^a} = \frac{1}{|\Gamma_I^a|} \int_{\Gamma_I^a} c_a \, ds, \quad \langle c_c \rangle_{\Gamma_I^c} = \frac{1}{|\Gamma_I^c|} \int_{\Gamma_c^c} c_c \, ds, \quad V_c = \frac{1}{|\Gamma_c|} \int_{\Gamma_c} \phi_c \, ds - \frac{1}{|\Gamma_a|} \int_{\Gamma_a} \phi_a \, ds.$$

Average concentrations and cell voltage vs time for *Case 1* and *Case 2* are presented in Fig. 6. We depict results for fine-scale solution by red color and for multiscale solution by blue color.

For numerical comparison of the fine-scale and multiscale solutions, we use relative L2 and energy errors for potential

$$\|e_{\phi}\|_{1} = \frac{\int_{\varOmega} (\phi_{h} - \phi_{H})^{2}}{\int_{\varOmega} \phi_{h}^{2}}, \quad \|e_{\phi}\|_{2} = \frac{a_{\phi}^{DG}(\phi_{h} - \phi_{H}, \phi_{h} - \phi_{H})}{a_{\phi}^{DG}(\phi_{h}, \phi_{h})},$$

and for concentration

$$\|e_c\|_1 = \frac{\int_{\Omega} (c_h - c_H)^2}{\int_{\Omega} c_h^2}, \quad \|e_c\|_2 = \frac{a_c^{DG}(c_h - c_H, c_h - c_H)}{a_c^{DG}(c_h, c_h)}$$

where ϕ_h , c_h are the fine-scale solutions and ϕ_H , c_H are the multiscale solutions.

In Tables 2 and 3, we show relative L_2 and energy errors for potential and concentration at final time for the *Case 1*. For calculations, we use two different types of coarse meshes: structured and unstructured with different number of the local domains. We observe that the coarse mesh with larger number of local domains gives better results. For example, for 24 boundary and 24 interior basis functions for concentration and 24 boundary and 5 interior basis functions for potential, give $0.15\% L_2$ error and 15.7% energy error for potential and $0.05\% L_2$ error and 37.8% energy error for concentration, when we use

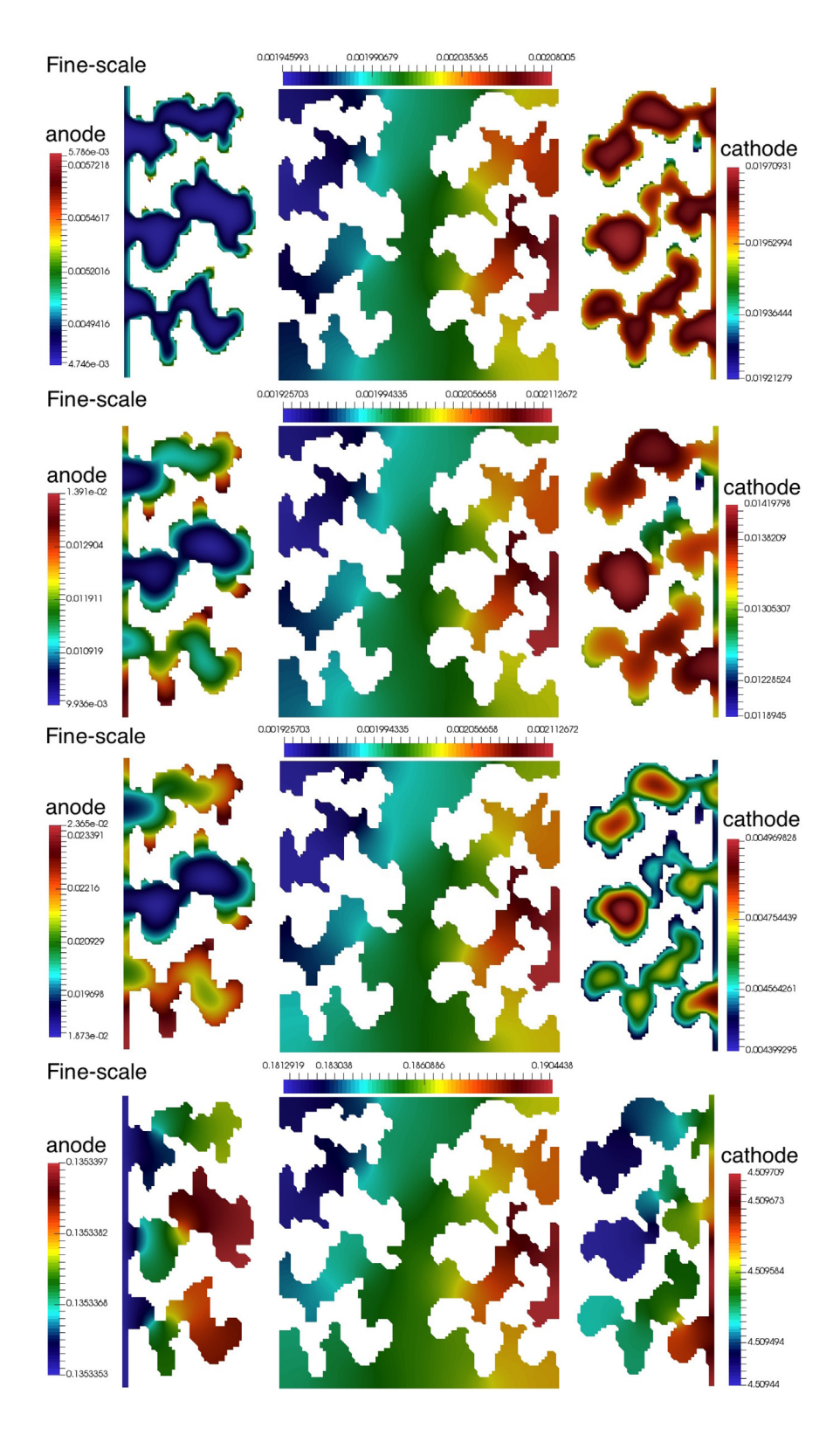


Fig. 5. Concentrations for different time t_m , m=10, 100 and 200 (first, second and third rows). Potential at final time (last row). Case 1. Fine-scale solution.

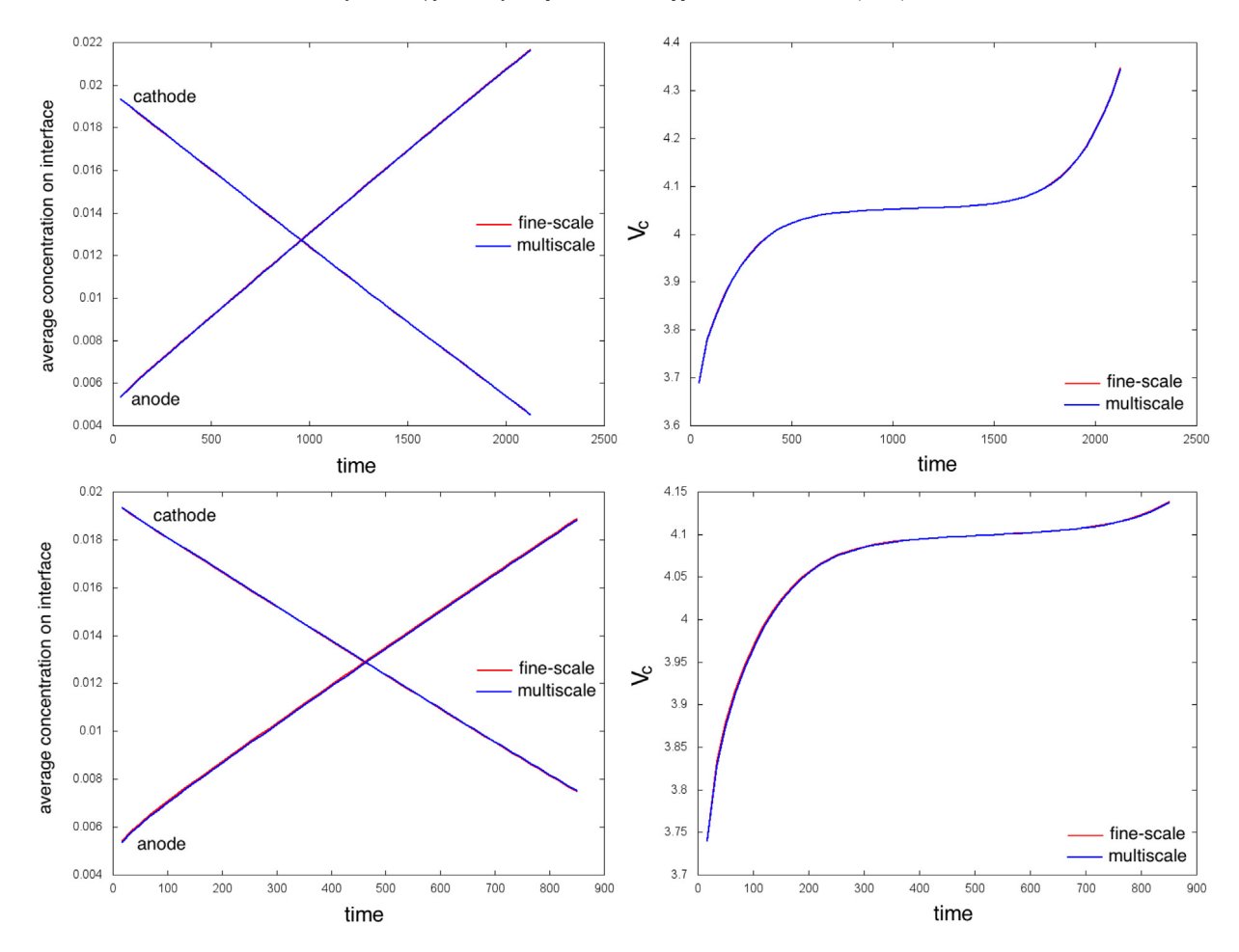


Fig. 6. Average concentration on Γ_l for anode and cathode vs time (left). Cell voltage V_c vs time (Right). Red color: fine-scale solution. Blue color: multiscale solution using structured coarse grid with 200 local domains. First row: Case 1. Second row: Case 2. (For interpretation of the references to colour in this figure legend, the reader is referred to the web version of this article.)

Table 2Numerical results of relative errors (%) at the final simulation time using structured coarse grid *Case 1*. Left: coarse mesh with 50 local domains. Right: coarse mesh with 200 local domains.

M_c^b	$\ e_\phi\ _1$	$\ e_\phi\ _2$	$\ e_c\ _1$	$\ e_c\ _2$	M_c^b	$\ e_{\phi}\ _1$	$\ e_{\phi}\ _2$	$\ e_c\ _1$	$\ e_c\ _2$	
$M_{\phi}^b = M_c^b$ and $M_{\phi}^i = 0$, $M_c^i = 0$					$M_{\phi}^{b} = \Lambda$	$M_{\phi}^b = M_c^b$ and $M_{\phi}^i = 0$, $M_c^i = 0$				
6	_	-	-	_	6	0.529	58.042	0.995	76.989	
8	0.603	57.154	1.004	86.443	8	0.440	40.350	0.522	68.278	
12	0.523	35.925	0.455	77.482	12	0.323	22.102	0.165	58.895	
16	0.462	23.610	0.235	72.264	16	0.287	15.239	0.100	54.885	
24	0.423	16.1455	0.173	68.734	24	0.264	9.245	0.083	52.697	
$M_{\phi}^{b} = N$	$M_{\phi}^{b} = M_{c}^{b}$ and $M_{\phi}^{i} = 5$, $M_{c}^{i} = M_{c}^{b}$					$M_{\phi}^b = M_c^b$ and $M_{\phi}^i = 5$, $M_c^i = M_c^b$				
6	_	_	_	_	6	0.407	57.511	0.976	65.815	
8	0.450	56.458	0.970	73.357	8	0.299	39.824	0.499	53.719	
12	0.324	34.814	0.394	58.331	12	0.142	21.375	0.125	37.705	
16	0.228	21.954	0.156	48.596	16	0.088	14.239	0.045	28.831	
24	0.155	15.705	0.056	37.836	24	0.052	7.5418	0.039	21.564	

coarse mesh with 50 local domains. When we use coarse mesh with 200 local domains, we can reduce errors approximately two times $(0.05\% L_2 \text{ error})$ and 7.5% energy error for potential and $0.03\% L_2 \text{ error}$ and 21.5% energy error for concentration). Relative errors for structured and unstructured meshes are similar. We note that, for the construction of the unstructured mesh we use standard mesh partitioner Metis. For the *Case 2*, we obtain similar results (see Table 4). In Fig. 7, we present relative L_2 and energy errors vs time for potential and concentration for the *Case 1*.

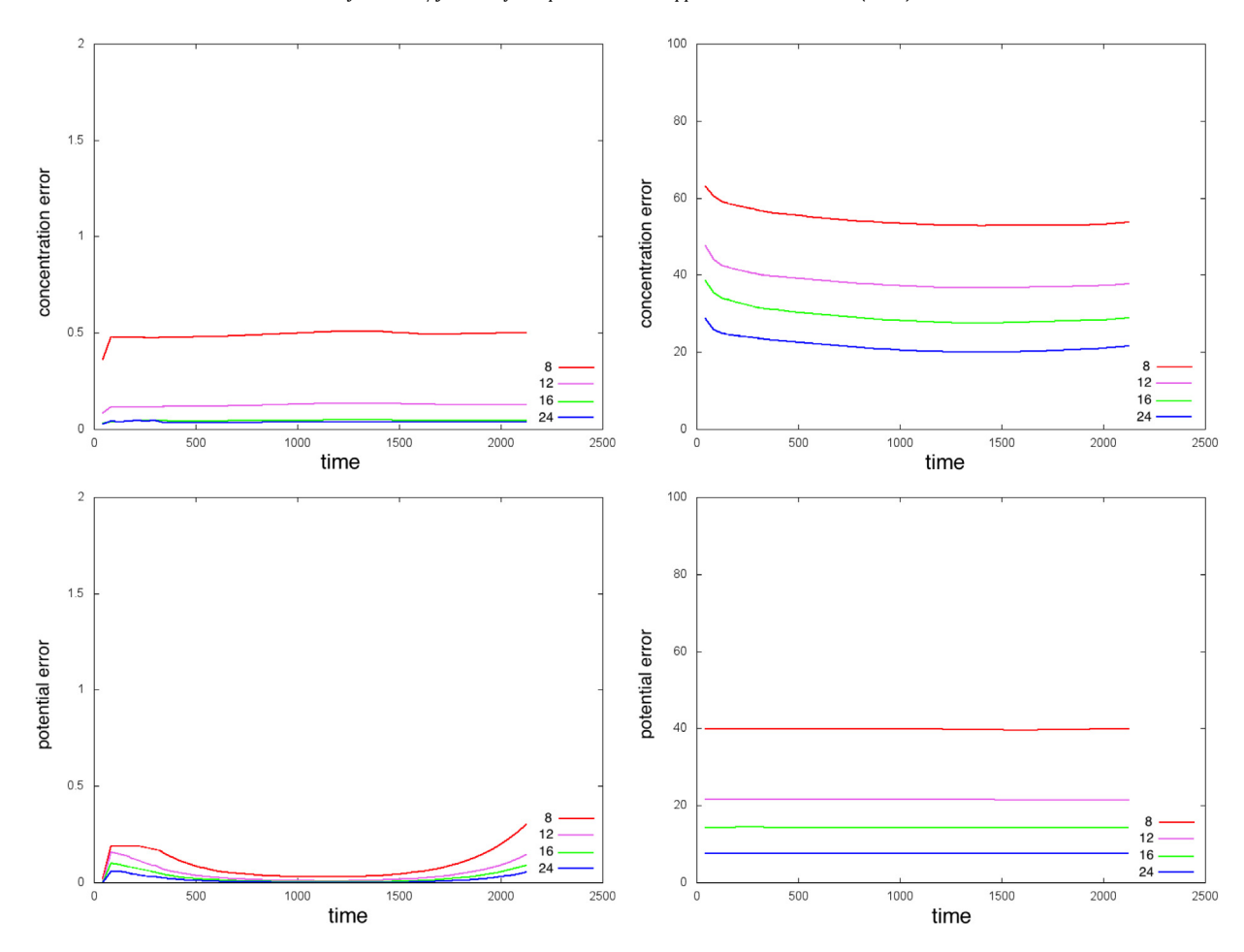


Fig. 7. Relative L_2 and energy errors (%) for concentration and potential vs time for structured coarse grid with 200 local domains for *Case 1* with different number of multiscale basis functions M_c^b and M_c^b . First row: errors for concentration for $M_\phi^b = M_c^b$ and $M_\phi^i = 5$, $M_c^i = M_c^b$. Second row: errors for potential for $M_\phi^b = M_c^b$ and $M_\phi^i = 5$, $M_c^i = M_c^b$. Left: relative L_2 error ($\|e_*\|_1$). Right: relative energy error ($\|e_*\|_2$).

Table 3Numerical results of relative errors (%) at the final simulation time using unstructured coarse grid *Case 1*. Left: coarse mesh with 50 local domains. Right: coarse mesh with 200 local domains.

M_c^b	$\ e_{\phi}\ _1$	$\ e_{\phi}\ _2$	$\ e_{c}\ _{1}$	$\ e_c\ _2$	M_c^b	$\ e_{\phi}\ _1$	$\ e_{\phi}\ _2$	$\ e_{c}\ _{1}$	$\ e_c\ _2$	
$M_{\phi}^{b} = M$	$M_{\phi}^b = M_c^b$ and $M_{\phi}^i = 0$, $M_c^i = 0$					$M^b_\phi=M^b_c$ and $M^i_\phi=0, M^i_c=0$				
6	0.644	75.400	1.489	90.504	6	0.538	60.789	1.132	75.984	
8	0.610	59.015	1.113	85.643	8	0.440	44.675	0.741	66.346	
12	0.545	36.533	0.604	79.671	12	0.335	24.817	0.261	58.540	
16	0.493	27.749	0.417	74.314	16	0.290	17.636	0.132	54.861	
24	0.448	17.174	0.219	71.512	24	0.253	10.226	0.079	52.381	
$M_{\phi}^{b} = M$	$M_{\phi}^b = M_c^b$ and $M_{\phi}^i = 5$, $M_c^i = M_c^b$ $M_{\phi}^b = M_c^b$					M_c^b and $M_\phi^i = 5$, M_c^b	$M_c^i = M_c^b$			
6	0.499	74.458	1.447	77.943	6	0.431	60.424	1.121	65.499	
8	0.439	57.788	1.065	69.214	8	0.311	44.257	0.728	52.597	
12	0.336	34.574	0.538	58.306	12	0.179	24.217	0.239	39.201	
16	0.248	25.265	0.333	48.279	16	0.115	16.827	0.097	31.079	
24	0.162	13.257	0.061	39.410	24	0.047	8.857	0.030	21.048	

Multiscale solver can significantly reduce the size of the system and provide accurate solutions. Construction of the multiscale solver can be divided into the offline and online stages. On offline stage ($Stage\ 1$) we solve local problems and construct multiscale basis functions. On online stage ($Stage\ 2$) we construct coarse grid approximation on multiscale space. We construct the multiscale basis functions only once as a precalculation. Next, we consider the computational advantages of our approach and consider the online computational cost. Let DOF_f^c and DOF_f^ϕ be the number of degrees of freedom for

Table 4Numerical results of relative errors (%) at the final simulation time using structured coarse grid with 200 local domains. *Case 2*.

M_c^b	$\ e_{\phi}\ _1$	$\ e_{\phi}\ _2$	$\ e_c\ _1$	$\ e_{c}\ _{2}$						
$M_{\phi}^{b}=M$	$M_\phi^b=M_c^b$ and $M_\phi^i=0, M_c^i=0$									
6	0.280	58.071	1.899	76.928						
8	0.205	40.243	1.004	67.921						
12	0.125	22.142	0.312	58.386						
16	0.098	15.220	0.186	54.277						
24	0.084	9.1870	0.154	51.993						
$M_{\phi}^{b} = M$	$M_{\phi}^b = M_c^b$ and $M_{\phi}^i = 5$, $M_c^i = M_c^b$									
6	0.236	57.579	1.869	66.012						
8	0.155	39.734	0.964	53.688						
12	0.063	21.470	0.244	37.612						
16	0.031	14.290	0.086	28.712						
24	0.014	7.602	0.043	21.234						

concentration and for potential on the fine grid, respectively. Let N_f be the number of cells on fine grid. Therefore for IPDG fine grid approximation then for two-dimensional problems and discontinuous Galerkin fine grid approximation, we have $DOF_f^c = DOF_f^\phi = 3N_f$ for triangular cells.

The number of degrees of freedoms for multiscale solver are DOF_{ms}^c for concentration and DOF_{ms}^ϕ for potential. The multiscale system size depends on the coarse-grid size and the number of local multiscale basis functions. Assume that N_c is the number of local domains (coarse grid cells). Therefore, for $M_c = M_c^b + M_c^i$ multiscale basis functions for concentration and $M_\phi = M_\phi^b + M_\phi^i$ for potential field in each local domain, we have $DOF_{ms}^c = N_c \cdot M_c$ and $DOF_{ms}^\phi = N_c \cdot M_\phi$ for concentration and potential, respectively. In general, the number of basis is independent of N_f i.e., a few basis functions can approximate the fine-scale solution accurately no matter how fine is the fine grid (very fine grid can be needed for complex pore-scale geometries).

Then, we can compare the computational cost of solving coarse and fine problems. For the fine-scale system on fine grid with $N_f=20,000$ triangular cells, we have $DOF_f^c=DOF_f^\phi=60\,000$. For example, for coarse grid with $N_c=200$ cells (local domains) with $M_\phi^b=M_c^b=24$ and $M_\phi^i=5$, $M_c^i=M_c^b$, the coarse-scale system size for concentration and potential are $DOF_{ms}^c=9600$ and $DOF_{ms}^\phi=5800$, respectively. Then, we can obtain good solution for multiscale solver using only 16% from DOF_{ms}^c for concentration and 9.6% from DOF_{ms}^ϕ with $\|e_c\|_1=0.03\%$ and $\|e_\phi\|_1=0.047\%$ for Case 1. In addition, we summarize a main point

- We studied a different number of multiscale basis functions (see Table 2). In GMsFEM instead of using classical finite
 element basis (polynomials), we use as basis local spectral problem solution in each coarse cell and couple them by
 IPDG framework. In this method by taking sufficient number (for convergence) of the multiscale basis functions, we
 can obtain good results.
- We constructed multiscale basis functions and perform calculations on different types of coarse grid: structured and unstructured (see Tables 2 and 3). Relative errors for structured and unstructured meshes are similar.
- We have considered a different number of the local domains (see Tables 2 and 3). We observe that the coarse mesh with larger number of local domains gives better results for both structured and unstructured coarse grids.
- We reduce errors by adding the interior basis functions (see Table 2). For concentration on structured coarse mesh with 200 local domains, we have 0.08% of L_2 error and 52.6% of energy error, when we take $M_c^b = 24$ boundary basis functions. After adding interior basis functions ($M_c^i = M_c^b$), we reduce errors to 0.03% of L_2 and 21.5% of energy errors. For potential, we have 0.2% of L_2 error and 9.2% of energy error, when we take $M_\phi^b = 24$ boundary basis functions. After adding interior basis functions ($M_\phi^i = M_\phi^b$), we reduce errors to 0.05% of L_2 and 7.5% of energy errors.
- We have performed the sensitivity of the error with respect to the parameter j_{app} and consider two cases, where we obtain similar results for both cases (see Table 4).

4. Conclusions

We presented multiscale model reduction for the pore-scale simulation of the Li-ion batteries. We proposed discontinuous Galerkin approximation for the problem with strong discontinuities and weakly impose nonlinear interface conditions. By discontinuous Galerkin approximation, we couple equations for electrolyte and solid domains via interface condition and write them as one equation in both domains with heterogeneous coefficients. Fine-scale approximation is constructed using information about variation of the solid medium in the micro level. We presented coarse-scale approximation using GMsFEM, where we avoid scale separation by construction of the multiscale basis functions with discontinuity on the interface and coupled them by IPDG framework. We performed numerical simulations for two cases with different i_{appl} and

consider structured and unstructured coarse grids with different number of multiscale basis functions. As in homogenization method, for extracting microstructure information we also perform calculation in local domains and use local solutions as a multiscale basis functions, but in presented multiscale method all calculations in the local domains are done offline. Numerical results show that the multiscale basis functions can efficiently capture the information of the fine-scale features of the medium with significant dimension reduction of the system and provide accurate solutions. In the future, we will consider online techniques and perform 3D calculations on high-performance computing systems and construct nonlinear multiscale basis functions for further reducing of the errors.

Acknowledgments

AM and PPM acknowledge financial support from NSF, USA, grant no. 1438431. MV's work is supported by the mega-grant of the Russian Federation Government (N 14.Y26.31.0013).

References

- [1] John B. Goodenough, Kyu-Sung Park, The Li-ion rechargeable battery: a perspective, J. Am. Chem. Soc. 135 (4) (2013) 1167-1176.
- [2] Elton J. Cairns, Paul Albertus, Batteries for electric and hybrid-electric vehicles, Annu. Rev. Chem. Biomol. Eng. 1 (2010) 299–320.
- [3] Michel Armand, J.-M. Tarascon, Building better batteries, Nature 451 (7179) (2008) 652-657.
- [4] Bruce Dunn, Haresh Kamath, Jean-Marie Tarascon, Electrical energy storage for the grid: a battery of choices, Science 334 (6058) (2011) 928–935.
- [5] M.N. Obrovac, V.L. Chevrier, Alloy negative electrodes for Li-ion batteries, Chem. Rev. 114 (23) (2014) 11444–11502.
- [6] James R. Wilson, J. Scott Cronin, Scott A. Barnett, Stephen J. Harris, Measurement of three-dimensional microstructure in a LiCoO 2 positive electrode, J. Power Sources 196 (7) (2011) 3443–3447.
- [7] P.R. Shearing, L.E. Howard, Peter Stanley Jørgensen, N.P. Brandon, S.J. Harris, Characterization of the 3-dimensional microstructure of a graphite negative electrode from a Li-ion battery. Electrochem. Commun. 12 (3) (2010) 374–377.
- [8] J.-M. Tarascon, Michel Armand, Issues and challenges facing rechargeable lithium batteries, Nature 414 (6861) (2001) 359-367.
- [9] J. Vetter, P. Novák, M.R. Wagner, C. Veit, K.-C. Möller, J.O. Besenhard, M. Winter, M. Wohlfahrt-Mehrens, C. Vogler, A. Hammouche, Ageing mechanisms in lithium-ion batteries, J. Power Sources 147 (1) (2005) 269–281.
- [10] M. Wohlfahrt-Mehrens, C. Vogler, J. Garche, Aging mechanisms of lithium cathode materials, J. Power Sources 127 (1) (2004) 58–64.
- [11] R. Spotnitz, J. Franklin, Abuse behavior of high-power, lithium-ion cells, J. Power Sources 113 (1) (2003) 81-100.
- [12] Aashutosh Mistry, Daniel Juarez-Robles, Malcolm Stein, Kandler Smith, Partha P. Mukherjee, Analysis of long-range interaction in lithium-ion battery electrodes, J. Electrochem. Energy Convers. Storage 13 (3) (2016) 031006.
- [13] Partha P. Mukherjee, Aashutosh Mistry, Ankit Verma, Porous media applications: Electrochemical systems, in: Modeling Transport Phenomena in Porous Media with Applications, Springer, 2017, p. 93.
- [14] Chia-Wei Wang, Ann Marie Sastry, Mesoscale modeling of a Li-ion polymer cell, J. Electrochem. Soc. 154 (11) (2007) A1035-A1047.
- [15] Bernardo Orvananos, Hui-Chia Yu, Martin Z. Bazant, Katsuyo Thornton, Simulations of Li-Ion intercalation dynamics in 3D microstructures, in: Meeting Abstracts, The Electrochemical Society, 2011, p. 750.
- [16] Vahur Zadin, Heiki Kasemägi, Alvo Aabloo, Daniel Brandell, Modelling electrode material utilization in the trench model 3D-microbattery by finite element analysis, J. Power Sources 195 (18) (2010) 6218–6224.
- [17] Anders Logg, Kent-Andre Mardal, Garth Wells, Automated Solution of Differential Equations by the Finite Element Method: The FEniCS book, Springer Science & Business Media, 2012.
- [18] Jonás D. De Basabe, Mrinal K. Sen, Mary F. Wheeler, Seismic wave propagation in fractured media: a discontinuous Galerkin approach, in: SEG Technical Program Expanded Abstracts 2011, Society of Exploration Geophysicists, 2011, pp. 2920–2924.
- [19] M. Taralov, O. Iliev, Three Dimensional Finite Element Simulations of Electrochemical Processes in Li-ion Batteries, ITWM Technical Report, 2012.
- [20] M. Taralov, V. Taralova, P. Popov, J. Zausch, O. Iliev, A. Latz, Report on Finite Elements Simulations of Electrochemical Processes in Li-ion Batteries with Thermic Effects, Berichte des Fraunhofer ITWM, 2012.
- [21] O. Iliev, P.E. Zakharov, Domain splitting algorithms for the Li-ion battery simulation, in: IOP Conference Series: Materials Science and Engineering, Vol. 158, No. 1, IOP Publishing, 2016, 012099.
- [22] John Newman, Karen E. Thomas-Alyea, Electrochemical Systems, John Wiley & Sons, 2012.
- [23] Pauline De Vidts, Ralph E. White, Governing equations for transport in porous electrodes, J. Electrochem. Soc. 144 (4) (1997) 1343–1353.
- [24] Partha P. Mukherjee, Sreekanth Pannala, John A. Turner, Modeling and simulation of battery systems, second ed., Wiley Online Library 2011, pp. 841–875.
- [25] John Newman, William Tiedemann, Porous-electrode theory with battery applications, AIChE J. 21 (1) (1975) 25–41.
- [26] Seongkoo Cho, Chien-Fan Chen, Partha P. Mukherjee, Influence of microstructure on impedance response in intercalation electrodes, J. Electrochem. Soc. 162 (7) (2015) A1202–A1214.
- [27] Kyle C. Smith, Partha P. Mukherjee, Timothy S. Fisher, Columnar order in jammed LiFePO 4 cathodes: ion transport catastrophe and its mitigation, Phys. Chem. Chem. Phys. 14 (19) (2012) 7040–7050.
- [28] Honghe Zheng, Gao Liu, Xiangyun Song, Paul Ridgway, Shidi Xun, Vincent S. Battaglia, Cathode performance as a function of inactive material and void fractions, J. Electrochem. Soc. 157 (10) (2010) A1060–A1066.
- [29] Lukas Zielke, Tobias Hutzenlaub, Dean R. Wheeler, Ingo Manke, Tobias Arlt, Nils Paust, Roland Zengerle, Simon Thiele, A combination of X-ray tomography and carbon binder modeling: Reconstructing the three phases of LiCoO2 Li-ion battery cathodes, Adv. Energy Mater. 4 (8) (2014).
- [30] G. Liu, H. Zheng, S. Kim, Y. Deng, A.M. Minor, X. Song, V.S. Battaglia, Effects of various conductive additive and polymeric binder contents on the performance of a lithium-ion composite cathode, J. Electrochem. Soc. 155 (12) (2008) A887–A892.
- [31] Stephen J. Harris, Peng Lu, Effects of inhomogeneities nanoscale to mesoscale on the durability of Li-ion batteries, J. Phys. Chem. C 117 (13) (2013) 6481–6492.
- [32] Dirk Kehrwald, Paul R. Shearing, Nigel P. Brandon, Puneet K. Sinha, Stephen J. Harris, Local tortuosity inhomogeneities in a lithium battery composite electrode, J. Electrochem. Soc. 158 (12) (2011) A1393–A1399.
- [33] Charles Monroe, John Newman, Dendrite growth in lithium/polymer systems a propagation model for liquid electrolytes under galvanostatic conditions, J. Electrochem. Soc. 150 (10) (2003) A1377–A1384.
- [34] Hee Jung Chang, Andrew J. Ilott, Nicole M. Trease, Mohaddese Mohammadi, Alexej Jerschow, Clare P. Grey, Correlating microstructural lithium metal growth with electrolyte salt depletion in lithium batteries using 7Li MRI, J. Am. Chem. Soc. 137 (48) (2015) 15209–15216.

- [35] Georg Bieker, Martin Winter, Peter Bieker, Electrochemical in situ investigations of SEI and dendrite formation on the lithium metal anode, Phys. Chem. Phys. 17 (14) (2015) 8670–8679.
- [36] Magali Gauthier, Thomas J. Carney, Alexis Grimaud, Livia Giordano, Nir Pour, Hao-Hsun Chang, David P. Fenning, Simon F. Lux, Odysseas Paschos, Christoph Bauer, et al., Electrode–electrolyte interface in Li-ion batteries: Current understanding and new insights, J. Phys. Chem. Lett. 6 (22) (2015)
- [37] Francesco Ciucci, Wei Lai, Derivation of micro/macro lithium battery models from homogenization, Transp. Porous Media 88 (2) (2011) 249–270.
- [38] Marc Doyle, Thomas F. Fuller, John Newman, Modeling of galvanostatic charge and discharge of the lithium/polymer/insertion cell, J. Electrochem. Soc. 140 (6) (1993) 1526–1533.
- [39] Vasilena Taralova, Oleg Iliev, Yalchin Efendiev, Derivation and numerical validation of a homogenized isothermal Li-ion battery model, J. Eng. Math. 101 (1) (2016) 1–27.
- [40] E. Chung, Y. Efendiev, W.T. Leung, An adaptive generalized multiscale discontinuous Galerkin method (GMsDGM) for high-contrast flow problems, 2014. arXiv preprint arXiv:1409.3474.
- [41] Eric T. Chung, Yalchin Efendiev, Wing Tat Leung, Residual-driven online generalized multiscale finite element methods, J. Comput. Phys. 302 (2015) 176–190
- [42] Mario Ohlberger, Stephan Rave, Felix Schindler, Model reduction for multiscale lithium-ion battery simulation, 2016. arXiv preprint arXiv:1602.08910.
- [43] Zhe Li, Jun Huang, Bor Yann Liaw, Jianbo Zhang, On state-of-charge determination for lithium-ion batteries, J. Power Sources 348 (2017) 281–301.
- [44] Béatrice Rivière, Discontinuous Galerkin Methods for Solving Elliptic and Parabolic Equations: Theory and Implementation, Society for Industrial and Applied Mathematics, 2008.
- [45] D.N. Arnold, F. Brezzi, B. Cockburn, L.D. Marini, Unified analysis of discontinuous Galerkin methods for elliptic problems, SIAM J. Numer. Anal. 39 (5) (2001/02) 1749–1779.
- [46] Eric Chung, Yalchin Efendiev, Thomas Y. Hou, Adaptive multiscale model reduction with generalized multiscale finite element methods, J. Comput. Phys. 320 (2016) 69–95.
- [47] Y. Efendiev, T. Hou, Multiscale Finite Element Methods: Theory and Applications, Springer, 2009.
- [48] Y. Efendiev, T. Hou, V. Ginting, Multiscale finite element methods for nonlinear problems and their applications, Commun. Math. Sci. 2 (2004) 553–589.
- [49] Y. Efendiev, J. Galvis, T. Hou, Generalized multiscale finite element methods, J. Comput. Phys. 251 (2013) 116-135.
- [50] Eric T. Chung, Wing Tat Leung, Maria Vasilyeva, Yating Wang, Multiscale model reduction for transport and flow problems in perforated domains, J. Comput. Appl. Math. 330 (2018) 519–535.
- [51] Eric T. Chung, Yalchin Efendiev, Wing Tat Leung, Maria Vasilyeva, Yating Wang, Online adaptive local multiscale model reduction for heterogeneous problems in perforated domains, Appl. Anal. 96 (12) (2017) 2002–2031.
- [52] Eric T. Chung, Wing Tat Leung, Maria Vasilyeva, Mixed GMsFEM for second order elliptic problem in perforated domains, J. Comput. Appl. Math. 304 (2016) 84–99.
- [53] E.T. Chung, O. Iliev, M.V. Vasilyeva, Generalized multiscale finite element method for non-Newtonian fluid flow in perforated domain, in: Application of Mathematics in Technical and Natural Sciences: 8th International Conference for Promoting the Application of Mathematics in Technical and Natural Sciences, Vol. 1773, No. 1, AMiTaNS16, AIP Publishing, 2016, 100001.
- [54] E.T. Chung, Y. Efendiev, G. Li, M. Vasilyeva, Generalized multiscale finite element method for problems in perforated heterogeneous domains, Appl. Anal. 255 (2015) 1–15.